PAPER

Check for updates

A copper bromide-decorated magnetic oyster shell biosupport as a sustainable catalyst for heterogeneous synthesis of imidazo[1,2-*a*]pyridines in glycerol

Samane Ansari,† Arefe Salamatmanesh, [iD] †* Maryam Kazemi Miraki [iD] and Akbar Heydari [iD] *

Oyster shells (OSs) are a kind of biomineralized material derived from renewable resources, comprising calcium carbonate (>95 wt%) as the main component, organic moieties, and trace elements, which are often discarded haphazardly as waste. Due to their notable properties, OSs have been widely employed as templates or precursors in the synthesis of different functional nanomaterials. The acidic hydrolysis of the matrix proteins present in the OS structure produces an acid-cured OS powder (AOS) containing coordination sites −COOH and −NH$_2$, which can be used as a bed to immobilize catalytic metal species. In this context, we focused on utilizing acid-pretreated waste OS to stabilize copper bromide, which was subsequently combined with magnetite nanoparticles. The copper bromide-supported magnetic AOS was well characterized using various analyses, such as FT-IR, XRD, FE-SEM, EDX elemental mapping, TEM, ICP-OES, TGA, BET, and VSM. Then, the Cu-incorporated magnetic catalyst was successfully applied for the synthesis of a variety of imidazo[1,2-*a*]pyridine derivatives in glycerol as a green and sustainable medium. The synergistic effect of metallic Lewis acid and hydrogen bonding between the precursors and glycerol led to the production of desirable products in high yields. Furthermore, the catalyst can be easily synthesized and recovered.

1. Introduction

Oysters—as a family of common shellfish—are one of the critical aquaculture products in numerous coastal nations, and have been recognized for their considerable nutritional and economic value. Within the aquaculture sector, as well as in industries related to oyster processing and catering, a significant volume of OS is left unused, leading to both sustainable resource wastage and great environmental contamination.[1,2] A promising and cost-effective approach to waste management and pollution reduction is to recycle and convert bio-waste into value-added products by using them as templates or supports for developing heterogeneous catalysts.[3,4] Currently, biomaterials, as naturally available sources, have garnered significant interest among researchers due to their prominent features, including large specific surface areas and surface functional groups in addition to high biocompatibility, easy accessibility, environmental sustainability, and cost-effectiveness, making them ideal for the immobilization of active metal species and

the development of recoverable catalysts.[3,5] The direct utilization of bio-wastes as a substrate for loading nanoparticles without any pretreatment often represents a significant challenge due to the relatively inert nature of their surface, especially in the case of shell biomass. A prime example of this is the oyster shell, which is a naturally occurring biomineralized material composed of a significant amount of calcium carbonate (>95 wt%), a small amount of organic moieties, and trace elements. However, given that the OS structure includes organic matter (*e.g.*, proteins), it is plausible that the OS surface could be enhanced through chemical treatments.[6] The hydrolysis of the peptide bonds of the matrix proteins present in the OS structure (roughly 3.75 wt%) under acidic conditions, yielding both amino and carboxyl groups, is an efficient way to promote surface interaction with various catalytic species.[7,8]

Imidazo[1,2-*a*]pyridine scaffolds are found in numerous pharmaceuticals and biologically active natural products exhibiting antiviral,[9] antibacterial,[10] fungicidal, and anti-inflammatory[11] properties. Nowadays, there are many commercially available imidazo[1,2-*a*]pyridine-based drugs such as alpidem,[12,13] olprinone (a cardiotonic agent),[14] minodronic acid,[15] zolpidem,[16,17] nicopidem and saripidem (anxiolytic agents),[18,19] zolimidine (a gastroprotective agent),[20] and rifaximin (an antibiotic).[21] The inherent pharmacological and

Chemistry Department, Tarbiat Modares University, P.O. Box 14155-4838, Tehran, Iran. E-mail: heydar_a@modares.ac.ir; salamatmanesh.ar@gmail.com; Fax: +98-21-82883455; Tel: +98-21-82883444

† These authors contributed equally.

biological attributes of imidazo[1,2-a]pyridine frameworks have stimulated the advancement of efficient and mild synthetic strategies. Considerable efforts have been directed towards achieving the effective synthesis of these structures.[22] Nonetheless, the high costs and laborious multi-step procedures associated with the production of imidazo[1,2-a]pyridine derivatives have typically restricted the practical use of some of these techniques. After the pioneering report by Gevorgyan and Chernyak on a copper [CuCl/Cu(OTf)$_2$]-catalyzed three-component coupling reaction involving aldehydes, 2-aminopyridines, and terminal alkynes for the synthesis of imidazo[1,2-a]pyridines, a wide range of synthetic approaches have been introduced based on the utilization of different homogeneous and heterogeneous catalytic systems.[23–26] Despite their efficacy, some of these techniques face significant challenges, such as inadequate product yields, the need for toxic organic solvents, limited substrate diversity, lengthy reaction times, and the use of costly and non-recyclable catalysts. Therefore, it is imperative to develop an efficient sustainable catalytic system for the preparation of imidazo[1,2-a]pyridines using readily accessible and cost-effective materials.

Considering the previous reports and our persistent efforts towards the design of magnetic nanocatalysts alongside the development of sustainable organic transformations,[27–29] we hereby disclose the one-pot synthesis of imidazo[1,2-a]pyridines via three-component reactions of 2-aminopyridines, aldehydes, and alkynes, employing a sustainable heterogeneous catalytic system made up of magnetically recyclable acid-cured oyster shell (AOS) powder adorned by copper bromide species, and glycerol medium.

2. Experimental

2.1. Materials and methods

All required materials were purchased from Merck and Aldrich chemical companies and employed directly without any purification. The reaction was accurately monitored through thin-layer chromatography (TLC). All reported yields are isolated yields. Preparative TLC was carried out on glass plates coated with a thin layer of silica gel 60 F-254 (0.2 mm). The ^{1}H NMR and ^{13}C NMR spectra were obtained using a Bruker Avance (DRX 300 and 500 MHz) in pure deuterated CDCl$_3$ solvent, with tetramethylsilane (TMS) serving as the internal standard. Infrared spectra (IR) were obtained within the 400–4000 cm^{-1} range using the KBr pellet method on a NICOLET FT-IR 100 spectrometer. The catalyst's morphology and size were analyzed using scanning electron microscopy (SEM) with TESCAN MIRA III FE-SEM apparatus. Additionally, energy dispersive X-ray spectroscopy (EDX) was conducted alongside SEM to analyze the elemental composition of the particles. The X-ray diffraction (XRD) data were acquired at room temperature using a Philips PW1730 diffractometer with Cu Kα radiation ($\alpha = 1.54060$ Å), 30 mA current, 40 kV voltage, and a scanning rate of 0.05° s^{-1} across the 2θ range of 10–80°. TEM images were recorded using a transmission electron microscopy (TEM, Philips model CM300) instrument. A thermal analyzer (SDT Q600) was utilized at a heating rate of 20 °C min^{-1} to perform thermal gravimetric

analysis (TGA) within a temperature range of 25–800 °C, while argon was continuously flowing. To achieve magnetic saturation of the nanoparticles, a vibrating magnetometer/alternating gradient force magnetometer (VSM/AGFM, MDK Co., Iran) was employed. The BET (Brunauer–Emmett–Teller) surface area of the synthesized material was assessed through nitrogen gas physisorption data obtained using BELSORP MINI II apparatus at a temperature of 77 K. An inductively coupled plasma (ICP) analysis was executed utilizing a Varian Vista-Pro ICP-OEs spectrometer.

2.2. Preparation of the AOS powder

The oysters were sourced from a commercial farm located in the southern region of Iran. First, 4 g of OS powder was added to ethanol (20 mL) and sonicated for 10 min, and then the mixture was stirred for 20 min at 40 °C to facilitate complete dispersion. The acidic solution, including 16 mmol of stearic acid in ethanol (70 mL), was added to the reaction flask, and the pH should be around 4. Then, the reaction mixture was stirred at 40 °C for 2 h to complete the hydrolysis. Finally, the mixture was centrifuged, and the residue was washed twice with ethanol and dried at 70 °C for 7 h to afford the acid-cured oyster shell powder.

2.3. Preparation of the MNP@AOS structure

In a round-bottomed flask, 0.4 g of AOS powder was dispersed in 50 mL of deionized water using ultrasonic waves. Then, 1.84 mmol of FeCl$_3$·6H$_2$O and 0.92 mmol of FeCl$_2$·4H$_2$O were added to the flask, and the mixture was sonicated for 10 min followed by stirring for 30 min at 80 °C under an argon atmosphere. At this stage, 7 mL of ammonia solution (25% w/w) was added dropwise to the reaction mixture to adjust the pH of the solution to about 11, and the black solution was refluxed for 3 h under an argon atmosphere to produce modified magnetite nanoparticles. Finally, the magnetically separable OS powder was washed several times with water and ethanol and placed in an oven at 70 °C for 7 h to dry completely.

2.4. Preparation of the MNP@AOS-CuBr catalyst

To prepare the final catalyst, 10 mL of acetonitrile was added to a mixture of 0.2 g CuBr and 1 g of magnetically separable OS powder (obtained from stage 1) and sonicated for 10 min. Subsequently, 20 mL of DMF was added to the mixture and refluxed for 6 h. Finally, the resulting nanoparticles were washed twice with ethanol and dried in an oven at 80 °C for 3 h.

2.5. General procedure for the synthesis of imidazo[1,2-a] pyridine derivatives

In a test tube fitted with a stir bar, a combination of benzaldehyde (1.05 mmol) and 2-aminopyridine (1.0 mmol) was stirred for 15 to 20 min (in some cases, in the presence of glycerol at 100 °C). Following this, phenyl acetylene (1.1 mmol), 25 mg of MNP@AOS-CuBr (0.7 mol%) and glycerol solvent (2 mL) were introduced into the reaction tube. The mixture was then heated at 110 °C for a sufficient time while stirring. Upon completion of

the reaction, as determined by TLC, the reaction mixture was allowed to cool to room temperature and was diluted with 2 mL of water before magnetic filtration of the catalyst. The filtrate was extracted with EtOAc (20 mL × 3). After removal of the combined organic phases under reduced pressure, the crude product was purified by column chromatography on silica gel. The catalyst was recovered after washing with water and ethanol and subsequently drying in an oven.

3. Results and discussion

Catalyst synthesis consists of 3 steps as follows (Scheme 1): acid hydrolysis of the OS powder, functionalization of the AOS powder with magnetite nanoparticles, and immobilization of copper bromide on the magnetically recyclable acid-cured OS powder. The use of the Fe_3O_4-functionalized OS powder as a magnetic biosupport for stabilizing catalytic copper species due to its outstanding properties, including significant specific surface area along with surface functional groups, low toxicity, and easy recovery, leads to the production of a highly efficient and environmentally friendly heterogeneous copper(I) catalyst that has higher activity and stability than its homogeneous counterpart.[5,30] The structure of the resulting products was characterized using various methods, such as X-ray diffraction (XRD), infrared spectroscopy (FT-IR), thermal decomposition analysis (TGA), scanning electron microscopy (SEM), transmission electron microscopy (TEM), energy dispersive X-ray (EDX) analysis, specific surface area measurement (BET) analysis, and vibrating sample magnetometer (VSM) analysis.

3.1. Catalyst characterization

Fig. 1 shows the infrared (IR) spectra of the different stages of catalyst synthesis. The main absorption bands observed in the infrared spectrum of OS powder, as shown at Fig. 1a, correspond to the stretching vibration of the carbonate at 1426 cm^{-1} and the bending vibrations of the carbonate at 878 and 713 cm^{-1}, as well as the stretching vibrations of the C–H bonds of the methyl and methylene groups in the present protein structure at 2858 and 2928 cm^{-1}. The absorption peak corresponding to the protein C=O bond in the region of 1630 cm^{-1} overlapped with the peaks belonging to the carbonate species. No significant new peaks were observed in the infrared spectrum of the hydrolysed OS, indicating that the powder structure remained stable after acid hydrolysis. The intensity of the peaks in the range of 3300–
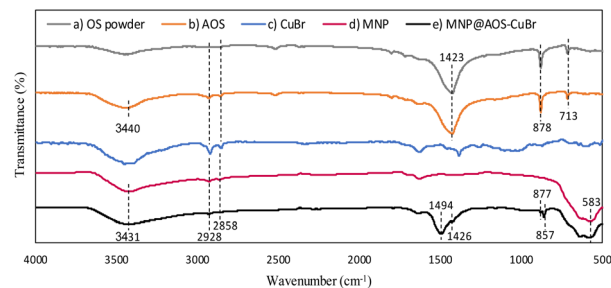
Fig. 1 The FT-IR spectra of OS powder (a), AOS powder (b), CuBr (c), MNP (d), and MNP@AOS-CuBr (e).

3500 cm^{-1} increased after acid hydrolysis, which can be attributed to the stretching vibrations of the OH and NH_2 groups, resulting from the hydrolysis of proteins in the OS structure. The modified magnetic powder has a strong peak at 583 cm^{-1}, which corresponds to the stretching vibration of the Fe–O bond. After immobilization of copper bromide on the magnetically recoverable acid-cured OS powder, the stretching vibration absorption peak at 3440 cm^{-1} was shifted to the lower wavenumber of 3431 cm^{-1}. Furthermore, the stretching vibration of the carbonate appeared at a higher wavenumber, as well as the bending vibration of the carbonate at a lower wavenumber.

The crystal structure of iron oxide nanoparticles, OS powder, CuBr, and MNP@AOS-CuBr was studied by X-ray diffraction analysis (Fig. 2). In the X-ray diffraction pattern of the iron oxide nanoparticles, the diffraction peaks observed at angles of 30.3°, 35.8°, 43.7°, 54.8°, 58.0° and 63.7° are associated with the (220), (311), (400), (422), (511) and (440) crystal planes, which are characteristic of iron oxide nanoparticles (JCPDS No. 629-19). As can be seen in the XRD pattern of the OS powder, the diffraction peaks located at 2θ = 23.28°, 29.24°, 36.40°, 39.26°, 43.25°, 47.74°, and 48.73° correspond to the (012), (104), (110), (113), (202), (024), and (116) planes of calcite (JCPDS 72-1652), demonstrating that the main component in the OS structure is calcium carbonate. The diffraction peaks related to calcite are also found in the XRD pattern of MNP@AOS-CuBr. Moreover, three new peaks appearing at angles of 25.6°, 42.4° and 50.1°, corresponding to the (111), (220) and (311) planes of copper bromide, along with the iron oxide diffraction peaks, are clearly
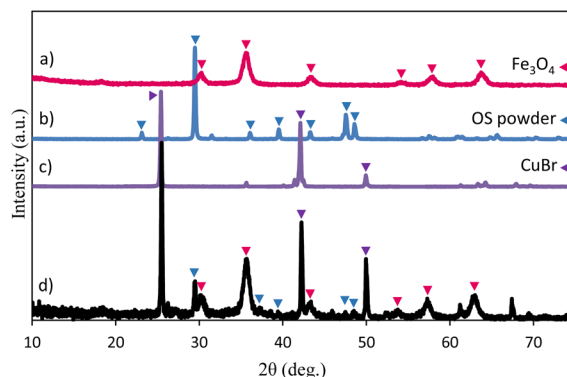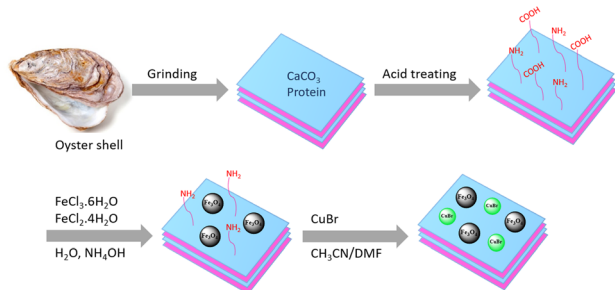

Scheme 1 Synthesis process of MNP@AOS-CuBr.

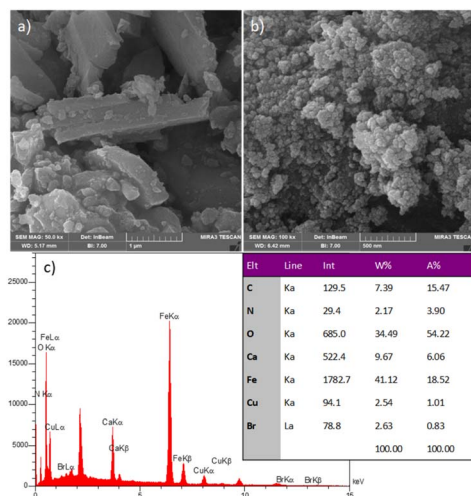**Fig. 2** The X-ray diffraction patterns of Fe_3O_4 (a), OS powder (b), CuBr (c), and MNP@AOS-CuBr (d).

Fig. 3 FE-SEM images of the OS powder (a), and MNP@AOS-CuBr. (b) EDX spectrum of MNP@AOS-CuBr (c).

visible in the diffraction pattern of the oyster shell modified with iron oxide nanoparticles and copper bromide. The appearance of these peaks indicates the successful immobilization of copper bromide species on the acid-cured OS powder functionalized with iron oxide nanoparticles.[3,31]

The surface morphology of the OS powder and MNP@AOS-CuBr has been studied using scanning electron microscopy analysis (Fig. 3). The SEM image in Fig. 3a shows that the OS powder has an irregular appearance and non-uniform particle size (0.1 to 10 μm). Meanwhile, MNP@AOS-CuBr has a uniform surface morphology that is homogeneously coated with magnetite nanoparticles. In addition, the aggregation and accumulation of the resulting nanostructure can be attributed to the magnetic nature of the Fe_3O_4 nanoparticles present in its composition (Fig. 3b). Energy dispersive X-ray spectroscopy analysis of the synthesized nanostructure proves the presence of the expected elements, including iron, carbon, nitrogen, calcium, oxygen, copper, and bromine (Fig. 3c).
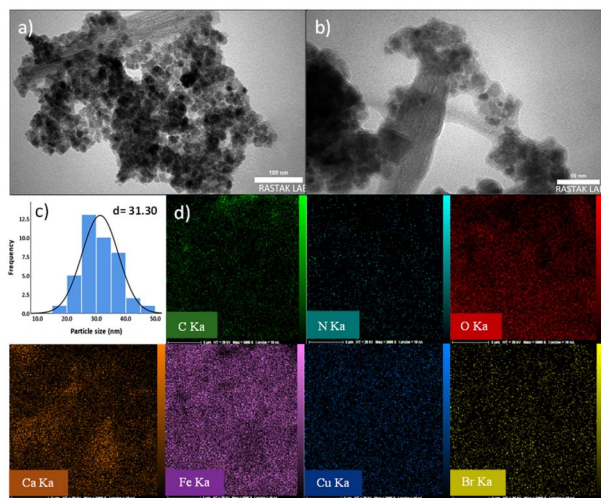
Fig. 4 TEM images of MNP@AOS-CuBr at different magnifications (a and b). Histogram of particle size distribution for MNP@AOS-CuBr (c). Element-mapping images of MNP@AOS-CuBr (d).
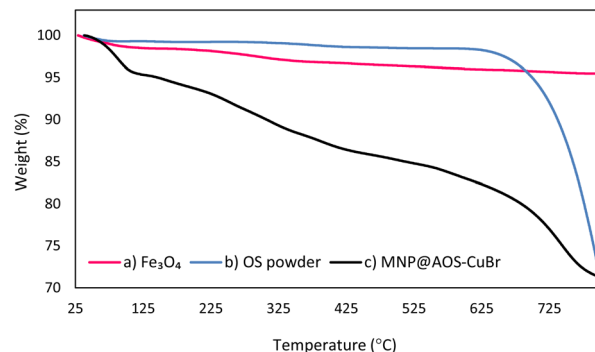
Fig. 5 TGA curves of Fe_3O_4 (a), OS powder (b), and MNP@AOS-CuBr (c).

The transmission electron microscope images of MNP@AOS-CuBr are presented at different magnifications in Fig. 4a and b. The relatively dark spherical spots represent iron oxide nanoparticles, while the light gray areas indicate OS particles. The particle size distribution for MNP@AOS-CuBr, which was obtained based on the TEM images, is shown in Fig. 4c. The average particle diameter (d) of the nanoparticles obtained from the statistical histogram was found to be 31.3 nm. In addition, Fig. 4d displays the density and distribution of the expected elements, namely iron, carbon, nitrogen, calcium, oxygen, copper, and bromine, found in the final nanostructure.

The thermal behaviour of the OS powder and MNP@AOS-CuBr was evaluated by thermogravimetric analysis (Fig. 5). The weight loss observed at temperatures below 150 °C is due to surface hydroxyl groups and physically adsorbed moisture. The weight loss before and after 575 °C can be attributed to the decomposition of organic fractions and pyrolysis of calcium carbonate, respectively. The final nanostructure containing hydrolysed oyster showed a greater weight loss than the original oyster at temperatures below 575 °C, which could be due to the formation of more organic groups with less stability on the oyster surface following acidic hydrolysis.

The copper content in the MNP@AOS-CuBr structure was evaluated to be 0.28 mmol g^{-1} using inductively coupled plasma analysis.

The magnetic properties of the MNP@AOS-CuBr and Fe_3O_4 nanoparticles were investigated using a vibration magnetometer (Fig. 6). According to the results obtained, the saturation value is
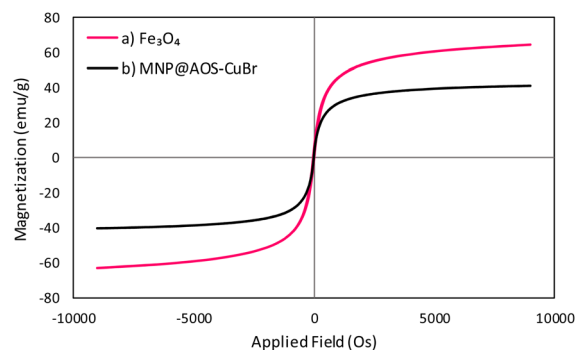
Fig. 6 Magnetization curves of Fe_3O_4 (a) and MNP@AOS-CuBr (b).
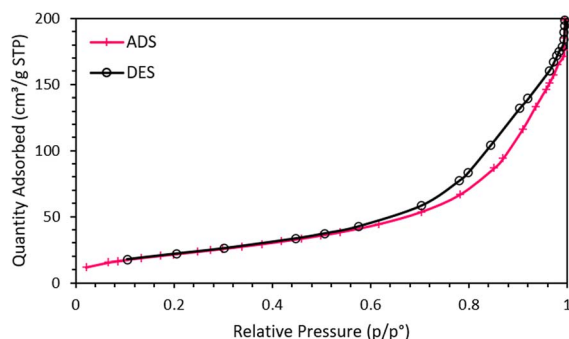
Fig. 7 N₂ adsorption–desorption isotherm of MNP@AOS-CuBr.

41.26 emu g^{-1} for the final nanoparticles and 63.9 emu g^{-1} for the magnetite nanoparticles. As a result, the magnetically recoverable Cu-incorporated AOS powder has superparamagnetic properties and can be easily separated by an external magnet.

The specific surface area of the magnetically recoverable Cu-incorporated AOS powder was measured by the BET method (Fig. 7). According to the results obtained from the nitrogen adsorption–desorption isotherm, the synthesized material has a specific surface area of 81.06 m^2 g^{-1}, a pore volume of 0.17 cm^3 g^{-1}, and a pore radius of 59.13 angstroms.

3.2. Catalytic activity

After identifying the fabricated materials, their catalytic performance was investigated in the synthesis of imidazo[1,2-a] pyridine derivatives. The study began by examining the reaction

between three components, namely benzaldehyde, 2-amino-pyridine, and phenylacetylene. As shown in Table 1, the effects of different solvents, the amount of catalyst, and temperature were investigated. At first, the model reaction was carried out both in the presence and absence of the catalyst in glycerol solvent at 110 °C, and the results revealed that the corresponding imidazo-[1,2-a]pyridine was successfully obtained in 93% yield when the magnetically recoverable Cu-incorporated acid-cured oyster shell was used as a catalyst, whereas the absence of the catalyst resulted in only a 10% yield of the desired product. In addition, performing the reaction in the presence of CuBr resulted in a low yield of 53%. Therefore, the immobilization of CuBr on the magnetically separable acid-cured OS powder causes the final heterogeneous copper(ı) catalyst to have better physicochemical features, higher stability, and consequently higher catalytic activity compared to homogeneous CuBr, in addition to easy recovery and reusability. The catalyst performance for the model reaction was investigated in various solvents, such as water, ethanol, a mixture of water and ethanol, dimethylformamide, toluene, polyethylene glycol (400, 600), and glycerol. The results indicated that the corresponding product was produced with the highest yield in glycerol solvent. Additionally, to investigate the required amount of the catalyst, the model reaction was repeated with different amounts of the catalyst, and the best result was acquired using 25 mg of the catalyst (0.7 mol%), while the reaction yield decreased to 68% with the use of 15 mg of the catalyst (0.42 mol%), and no significant increase was observed when 35 mg of the catalyst (0.98 mol%) was used. When the reaction temperature was changed to 100 °C, the yield

Table 1 Screening of the reaction conditions[a]

Ent.	Solvent	Temp.	Cat. (mol%)	Time (h)	Yield[b] (%)
1	Glycerol	110	CuBr	8	56
2	Glycerol	110	—	10	—
3	Glycerol	110	MNP@AOS-CuBr (0.70)	4	93
4	PEG 400	110	MNP@AOS-CuBr (0.70)	6	40
5	PEG 600	110	MNP@AOS-CuBr (0.70)	6	35
6	DMF	110	MNP@AOS-CuBr (0.70)	5	10
7	H₂O	100	MNP@AOS-CuBr (0.70)	8	Trace
8	H₂O/EtOH (1 : 1)	100	MNP@AOS-CuBr (0.70)	6	75
9	H₂O/CTAB[c]	110	MNP@AOS-CuBr (0.70)	6	Trace
10	Toluene	110	MNP@AOS-CuBr (0.70)	6	25
11	EtOH	80	MNP@AOS-CuBr (0.70)	6	70
12	—	80	MNP@AOS-CuBr (0.70)	12	30
13	Glycerol	110	MNP@AOS-CuBr (0.42)	4	68
14	Glycerol	110	MNP@AOS-CuBr (0.98)	4	93
15	Glycerol	100	MNP@AOS-CuBr (0.70)	4	70
16	Glycerol	120	MNP@AOS-CuBr (0.70)	4	94

[a] Reaction conditions: benzaldehyde (1.05 mmol), 2-aminopyridine (1.0 mmol), phenylacetylene (1.1 mmol) and different values of MNP@AOS-CuBr in solvent (2.0 mL). [b] Isolated yields. [c] 5 mg of CTAB.
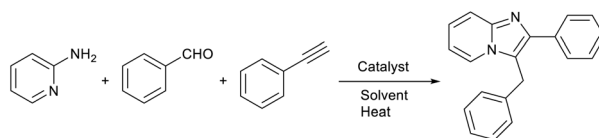
Table 2 Scope of the reaction of 2-aminopyridines with aldehydes and alkynes using MNP@AOS-CuBr[a]
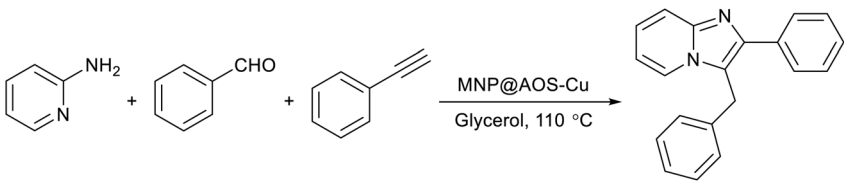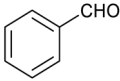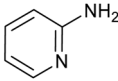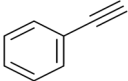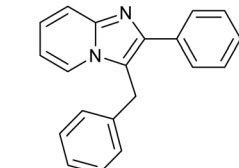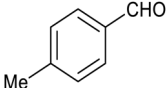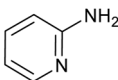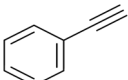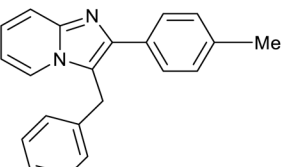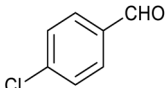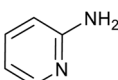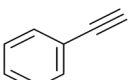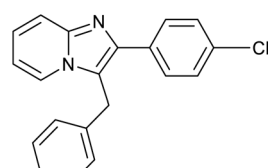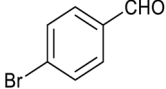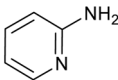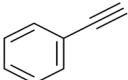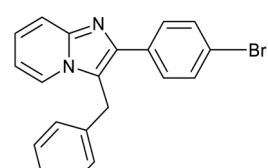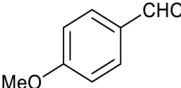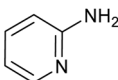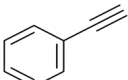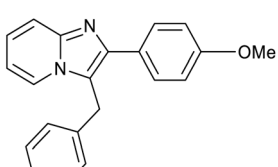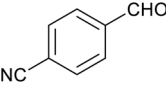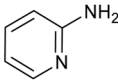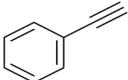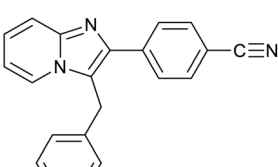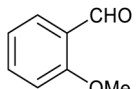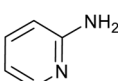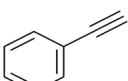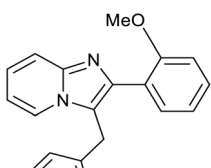
Entry	Aldehyde	2-Aminopyridine	Alkyne	Product	Yield[b] (%)	TON/TOF
1					93	133/33
2					87	124/31
3					85	121/30
4					83	119/30
5					90	129/32
6					65	93/23
7					76	109/27

Table 2 (*Contd.*)
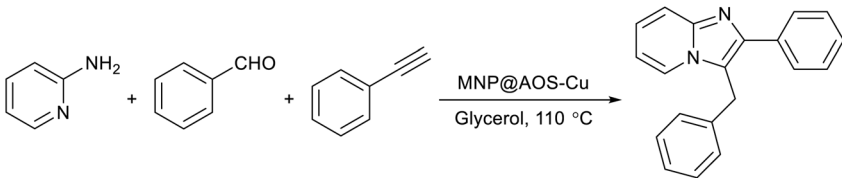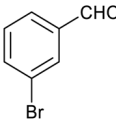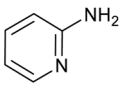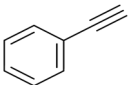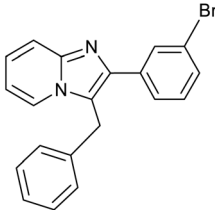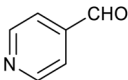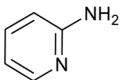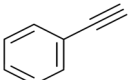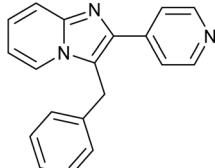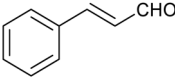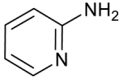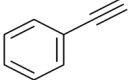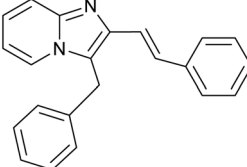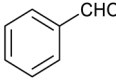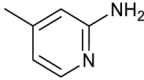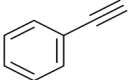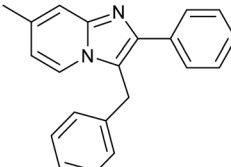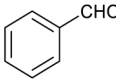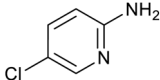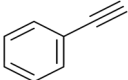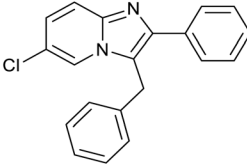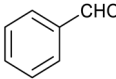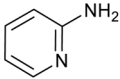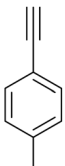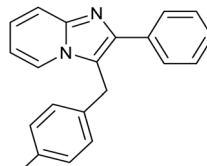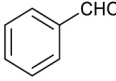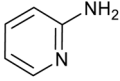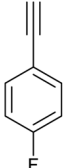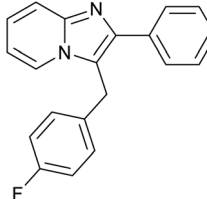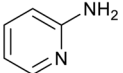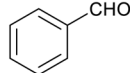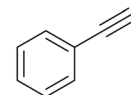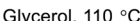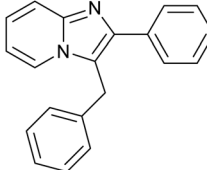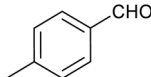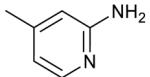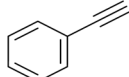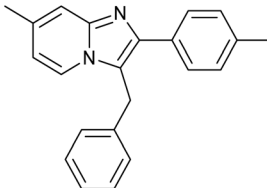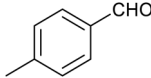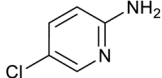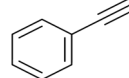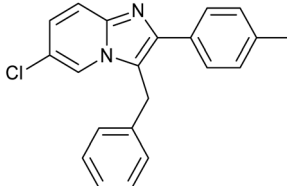
Entry	Aldehyde	2-Aminopyridine	Alkyne	Product	Yield[b] (%)	TON/TOF
8	3-Br-benzaldehyde	2-aminopyridine	phenylacetylene		81	116/29
9	pyridine-4-CHO	2-aminopyridine	phenylacetylene		74	106/26
10	cinnamaldehyde	2-aminopyridine	phenylacetylene		72	103/26
11	benzaldehyde	4-methyl-2-aminopyridine	phenylacetylene		85	121/30
12	benzaldehyde	5-Cl-2-aminopyridine	phenylacetylene		75	107/27
13	benzaldehyde	2-aminopyridine	4-methylphenylacetylene		80	114/28
14	benzaldehyde	2-aminopyridine	4-fluorophenylacetylene		85	121/30

Table 2 (*Contd.*)

Entry	Aldehyde	2-Aminopyridine	Alkyne	Product	Yield[b] (%)	TON/TOF
15					60	86/21
16					63	90/22

[a] Reaction conditions: 2-aminopyridine (1.0 mmol), aldehyde (1.05 mmol) and alkyne (1.1 mmol), 25 mg of MNP@AOS-CuBr (0.7 mol%) in glycerol (2.0 mL), 110 °C, 4 h. [b] Isolated yields.

of the desired product decreased to 70%, whereas no obvious change in yield was observed when the temperature was increased to 120 °C.

With the optimized conditions in hand, we explored the scope of the multicomponent method for various substituted 2-aminopyrindines, aldehydes and phenyl acetylene, and the results are presented in Table 2. The reaction conditions were tolerable for benzaldehydes with both electron-donating and electron-withdrawing substituents, as well as pyridine-4-carbaldehyde and cinnamaldehyde, and afforded the desired products in moderate to excellent yields. Aminopyridines bearing both electron-donating and electron-withdrawing groups (Me and Cl, respectively) gave the desired products in moderate and good yields. Furthermore, this transformation proceeded efficiently with various phenylacetylene derivatives, affording the corresponding products in good yields. The reaction between 4-methylbenzaldehyde and 2-aminopyridine derivatives bearing methyl and chlorine groups proceeded relatively smoothly to give the corresponding imidazo[1,2-a]pyridines in moderate yields. The tolerance of various functional groups in this protocol provides an opportunity for further chemical manipulation of the products.

A possible mechanism for the synthesis of imidazo[1,2-a] pyridines using the present approach has been proposed (Scheme 2). Initially, the formation of a Schiff base occurs through condensation of 2-aminopyridine and benzaldehyde, facilitated by glycerol through hydrogen-bond interactions. Then, copper(I) bromide species supported on the magnetic OS powder react with the alkyne to produce copper(I) acetylide, followed by the nucleophilic attack of the copper(I)-activated alkyne towards the imine to form the propargylamine intermediate. Finally, an intramolecular cyclization occurs via the nucleophilic attack of the pyridine ring nitrogen to the triple bond, activated with the supported copper(I) bromide species through a weak π-complex, and subsequently the aromatic isomerisation produces the corresponding product.[22,25,32]

3.3. Reusability of the catalyst

With respect to the foundations of green chemistry, the recyclability of the catalyst was examined (Fig. 8a). After completion of the model reaction, the reaction mixture was cooled to room temperature. Then, the catalyst was separated using a magnetic bar and washed with water and ethanol several times before drying at 70 °C for 7 h. The catalyst was reused in the model reaction 5 times without any significant decrease in activity. Additionally, the morphology of the retrieved MNP@AOS-CuBr catalyst was assessed using the FE-SEM technique (Fig. 8b). A comparison of the SEM images of both the fresh and recovered catalysts revealed that the structure and morphology of the catalyst were nearly preserved after the fifth run.
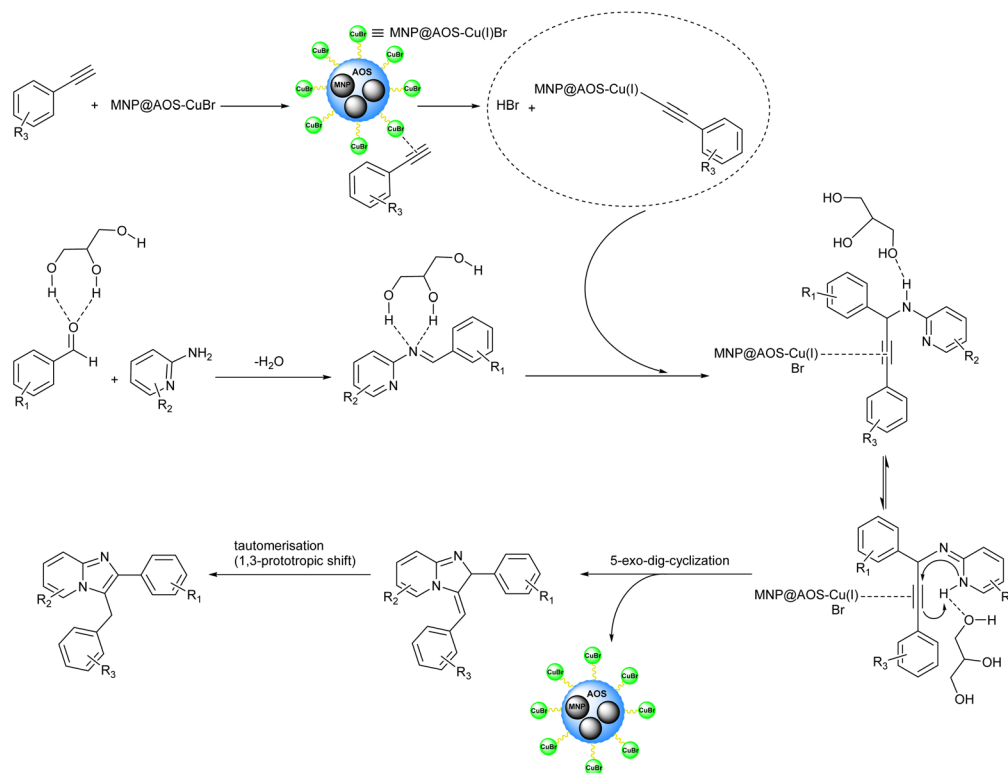
Scheme 2 Proposed mechanism for the synthesis of imidazo[1,2-a]pyridines from 2-aminopyridines, aldehydes and alkynes using MNP@AOS-CuBr.

Finally, to prove the heterogeneity of the prepared catalyst under the reaction conditions, a hot filtration test was used. In a typical experiment, the model reaction was carried out and stopped after 2 h. Then, the catalyst was magnetically removed from the reaction medium, and the reaction mixture was continuously stirred in the absence of the catalyst at 110 °C. No significant conversion was observed after 6 h, indicating that the leaching of Cu into the reaction mixture was negligible and that the present reaction proceeded *via* a heterogeneous catalytic process. Furthermore, the amount of Cu leaching was determined by ICP-OES analysis after five cycles and found to be only 0.52%.

3.4. Comparison study of catalytic activity

The performance and efficacy of the current methodology were evaluated against previous studies for the synthesis of imidazo [1,2-a]pyridines (Table 3). It is evident that employing the CuBr-incorporated magnetic catalyst, obtained from oyster shell as a biosupport, in a glycerol medium, has resulted in more favorable reaction conditions in terms of reaction duration and catalyst loading, leading to a corresponding product with a satisfactory yield. Additionally, the catalyst can be recovered and reused in subsequent cycles.
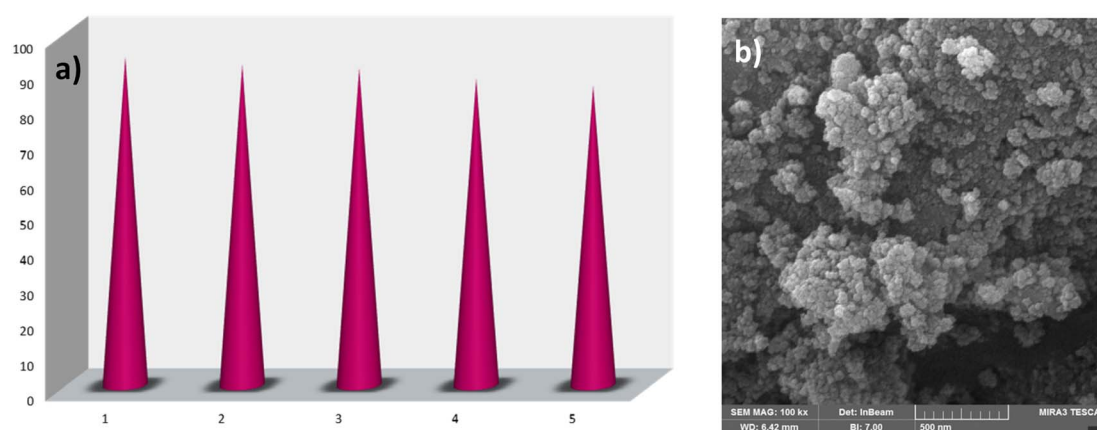

Fig. 8 Recycling of the MNP@AOS-CuBr catalyst in the synthesis reaction of 3-benzyl-2-phenylimidazo[1,2-a]pyridine (a) and FE-SEM image of the recovered MNP@AOS-CuBr (b).

Table 3 Comparison of the current protocol with other reported methods in the model reaction[a]

Entry	Catalyst (mol%)	Reaction conditions	Time (h)	Yield[b] (%)	Reference
1	CuCl (5 mol%)/Cu(OTf)$_2$ (5 mol%)	Toluene, 120 °C	16	92	23
2	CuI–NaHSO$_4$·SiO$_2$ (5 mol%)	Toluene, 110 °C, N$_2$	12	91	33
3	Cu–Mn (10 mol%)	H$_2$O, 100 °C	4	85	34
4	CuO/rGO (2.8 mol%)	DMSO, 110 °C	6	91	35
5	MNPs@BiimCu(I) (1.2 mol%)	H$_2$O, CTAB, 100 °C	5	92	36
6	CuSO$_4$ (10 mol%)/NaOAs (20 mol%)	H$_2$O, SDS, 50 °C	6	88	25
7	MNP@AOS-CuBr (0.7 mol%)	Glycerol, 110 °C	4	93	This work

[a] Three-component reaction between 2-aminopyridine, benzaldehyde and phenylacetylene. [b] Isolated yields.

4. Conclusions

To conclude, we successfully designed a novel, effective, and eco-friendly catalytic strategy that employs copper bromide immobilized on a magnetically retrievable biosupport, derived from oyster shell, for the one-pot synthesis of imidazo[1,2-*a*]pyridines in a glycerol medium through a three-component reaction involving 2-aminopyridines, aldehydes, and alkynes. The synergistic interaction between the MNP@AOS-CuBr catalyst and glycerol has led to the efficient production of the desired products in high yields. The MNP@AOS-CuBr can act as a Lewis acid in this reaction because of the existence of copper(I) bromide in its structure. The glycerol solvent can activate certain reaction precursors through hydrogen-bond interactions and bring them into proximity owing to its suitable polarity and solubility. The present catalyst system can be conveniently recycled *via* magnetic filtration and reused for a minimum of five reaction cycles without a notable decline in catalytic performance.

Author contributions

Samane Ansari: experimental work, investigation and data curation. Dr Arefe Salamatmanesh: methodology, investigation and data curation, supervised the research project, writing, review, and editing. Dr Maryam Kazemi Miraki: writing original draft. Prof. Akbar Heydari: review and supervised the research project.

Conflicts of interest

There are no conflicts to declare.

Data availability

The data that support the findings of this study are available in the article and the supplementary information (SI). Supplementary information is available. See DOI: https://doi.org/10.1039/d5na00818b.

Acknowledgements

References

1 C. O. Hong, S. Y. Kim, J. Gutierrez, V. N. Owens and P. J. Kim, *Biol. Fertil. Soils*, 2010, **46**, 491–498.

2 Y. H. Lee, S. M. A. Islam, S. J. Hong, K. M. Cho, R. K. Math, J. Y. Heo, H. Kim and H. D. Yun, *Biosci., Biotechnol., Biochem.*, 2010, **74**, 1517–1521.

3 X. Xiong, L. Cai, Y. Jiang and Q. Han, *ACS Sustain. Chem. Eng.*, 2014, **2**, 765–771.

4 N. Nakatani, H. Takamori, K. Takeda and H. Sakugawa, *Bioresour. Technol.*, 2009, **100**, 1510–1513.

5 X. Xiong, H. Chen and R. Zhu, *Chin. J. Catal.*, 2014, **35**, 2006–2013.

6 X. Liu, J. Dai, W. Li, K. Wang, J. Huang, Q. Li and G. Zhan, *ACS Sustain. Chem. Eng.*, 2019, **7**, 17768–17777.

7 X. Liu, G. Zhan, J. Wu, W. Li, Z. Du, J. Huang, D. Sun and Q. Li, *ACS Sustain. Chem. Eng.*, 2020, **8**, 7162–7173.

8 B. Penke, R. Ferenczi and K. Kovács, *Anal. Biochem.*, 1974, **60**, 45–50.

9 M. Lhassani, O. Chavignon, J.-M. Chezal, J.-C. Teulade, J.-P. Chapat, R. Snoeck, G. Andrei, J. Balzarini, E. De Clercq and A. Gueiffier, *Eur. J. Med. Chem.*, 1999, **34**, 271–274.

10 Y. Rival, G. Grassy and G. Michel, *Chem. Pharmaceut. Bull.*, 1992, **40**, 1170–1176.

11 K. C. Rupert, J. R. Henry, J. H. Dodd, S. A. Wadsworth, D. E. Cavender, G. C. Olini, B. Fahmy and J. J. Siekierka, *Bioorg. Med. Chem. Lett.*, 2003, **13**, 347–350.

12 N. Aditya, P. Shivkant, B. B. Sunil, J. Surabhi and S. Smriti, *Infect. Disord.: Drug Targets*, 2024, **24**, 16–41.

13 A. Cappelli, G. Giuliani, S. Valenti, M. Anzini, S. Vomero, G. Giorgi, C. Sogliano, E. Maciocco, G. Biggio and A. Concas, *Bioorg. Med. Chem.*, 2008, **16**, 3428–3437.

14 K. Mizushige, T. Ueda, K. Yukiiri and H. Suzuki, *Cardiovasc. Drug Rev.*, 2002, **20**, 163–174.

15 M. Tanaka, A. Hosoya, H. Mori, R. Kayasuga, H. Nakamura and H. Ozawa, *J. Bone Miner. Metabol.*, 2018, **36**, 54–63.

16 F. Dumont, R. N. Waterhouse, J. A. Montoya, F. Mattner, A. Katsifis, L. S. Kegeles and M. Laruelle, *Nucl. Med. Biol.*, 2003, **30**, 435–439.

17 M. Krause, H. Foks and K. Gobis, *Molecules*, 2017, **22**, 399.

18 R. Boerner and H. Moller, *Psychopharmakotherapie*, 1997, **4**, 145–148.

19 A. Garakani, J. W. Murrough, R. C. Freire, R. P. Thom, K. Larkin, F. D. Buono and D. V. Iosifescu, *Front. Psychiatr.*, 2020, **11**, 2020.

20 A. Deep, R. Kaur Bhatia, R. Kaur, S. Kumar, U. Kumar Jain, H. Singh, S. Batra, D. Kaushik and P. Kishore Deb, *Curr. Top. Med. Chem.*, 2017, **17**, 238–250.

21 H. L. DuPont, *Mini Rev. Med. Chem.*, 2016, **16**, 200–205.

22 A. K. Bagdi, S. Santra, K. Monir and A. Hajra, *Chem. Commun.*, 2015, **51**, 1555–1575.

23 N. Chernyak and V. Gevorgyan, *Angew. Chem., Int. Ed.*, 2010, **49**, 2743–2746.

24 W. Sun, W. Jiang, G. Zhu and Y. Li, *J. Organomet. Chem.*, 2018, **873**, 91–100.

25 Z. T. Bhutia, D. Das, A. Chatterjee and M. Banerjee, *ACS Omega*, 2019, **4**, 4481–4490.

26 P. Liu, L.-s. Fang, X. Lei and G.-q. Lin, *Tetrahedron Lett.*, 2010, **51**, 4605–4608.

27 A. Salamatmanesh and A. Heydari, *Appl. Catal., A*, 2021, **624**, 118306.

28 S. Mirshafiee, A. Salamatmanesh and A. Heydari, *Appl. Organomet. Chem.*, 2021, **35**, e6255.

29 A. Salamatmanesh, A. Heydari and H. T. Nahzomi, *Carbohydr. Polym.*, 2020, **235**, 115947.

30 X. Xiong and L. Cai, *Catal. Sci. Technol.*, 2013, **3**, 1301–1307.

31 X. Xiong, H. Chen, Z. Tang and Y. Jiang, *RSC Adv.*, 2014, **4**, 9830–9837.

32 G. K. Reen, A. Kumar and P. Sharma, *Beilstein J. Org. Chem.*, 2019, **15**, 1612–1704.

33 S. Mishra and R. Ghosh, *Synthesis*, 2011, **2011**, 3463–3470.

34 J. B. Bharate, S. K. Guru, S. K. Jain, S. Meena, P. P. Singh, S. Bhushan, B. Singh, S. B. Bharate and R. A. Vishwakarma, *RSC Adv.*, 2013, **3**, 20869–20876.

35 N. Hussain, P. Gogoi, M. R. Das, P. Sengupta, V. E. Fedorov, I. P. Asanov, M. N. Kozlova and S. B. Artemkina, *Appl. Catal., A*, 2017, **542**, 368–379.

36 M. Tajbakhsh, M. Farhang, R. Hosseinzadeh and Y. Sarrafi, *RSC Adv.*, 2014, **4**, 23116–23124.